Estimation of annual runoff using supraglacial channel geometry derived from UAV surveys of Qiyi Glacier, northern Tibetan Plateau

Longjiang Xie[1,2], Yuwei Wu[1,2], Ninglian Wang[1,2], Anan Chen[1,2,3], Shiqiang Zhang[1], and Sheng Hu[1]

[1]Shaanxi Key Laboratory of Earth Surface System and Environmental Carrying Capacity, College of Urban and Environmental Science, Northwest University, Xi'an 710127, China

[2]Qiyi Glacier Station, College of Urban and Environmental Science, Northwest University, Xi'an 710127, China

[3]National Cryosphere Desert Data Center, Northwest Institute of Eco-Environment and Resources, Chinese Academy of Sciences, Lanzhou 730000, China.

Correspondence to: Yuwei Wu (yuwei.wu@nwu.edu.cn), Sheng Hu (husheng@nwu.edu.cn)

Abstract. Due to difficulties in direct field observation and uncertainties in glacier runoff models, accurately estimating the glacier runoff remains one of the foremost challenges in cryospheric science. Using a digital elevation model (DEM) and orthophotos (both with a resolution of 5 cm) obtained from an unmanned aerial vehicle (UAV), this study developed a novel remote sensing method for estimating the annual discharge of the supraglacial channel over Qiyi Glacier in the northern Tibetan Plateau, which contributes to the majority of the glacier runoff. Our results showed that the catchment areas of the six main supraglacial channels covered 92.02% of the total glacier area and transported 89.43% of the annual surface meltwater yield (each ranging from 0.07×10^6 to 0.66×10^6 m^3). Some geometric parameters of the supraglacial channels (including lateral deviation, gradient, and width) were selected to predict the annual discharge using a stepwise regression model, which explained ~78.2% of the variance in the measurement-based glacier annual discharge, with the explained variance increasing to 81.8% after five-point moving average filtering. In comparison, a nonlinear regression model incorporating only the lateral deviation and specific gradient, which were more easily obtained practically, performed somewhat less well, accounting for 66.2% of the discharge variation; however, the explained variance increased to 81.4% after five-point filtering. If satellite remote sensing data with meter-level spatial resolution are available for a specific glacier research area, our regression models, based solely on the UAV-derived supraglacial channel network, will be a promising solution for monitoring changes in annual glacier discharge.

1 Introduction

In the context of global warming, most mountain glaciers worldwide are suffering from accelerated retreat with substantial influences on the glacier-fed rivers, especially for the "water tower of Asia" (Tibetan Plateau), which seriously threatens the livelihoods of hundreds of millions of people downstream with rising risks to water resource safety (Bolch et al., 2012; Huss, 2011; Immerzeel et al., 2020; Nie et al., 2021; Wang et al., 2021; Yao et al., 2022; Zemp et al., 2019). Emergent remote sensing data from different types of spaceborne sensors have been widely used to study various aspects of the influence of climate change on glaciers (Paul et al., 2015; Xu et al., 2025), such as glacier area (Burns and Nolin, 2014), ice mass change (Curran

33 et al., 2025; Kääb et al., 2012), equilibrium line altitude (ELA) (Rabatel et al., 2013), glacier surface velocity (Dehecq et al.,

34 2019; Kraaijenbrink et al., 2016), and glacier surface temperature (Ren et al., 2024; Wu et al., 2019). However, there is still a

35 lack of remote sensing retrieval methods for glacier runoff that link glacier changes directly to the water supply for downstream

36 human communities, which has become a major obstacle for understanding the patterns of glacier runoff changes for practical

37 water resource management and policy-making at the watershed or larger scale.

38 The supraglacial stream and channel network, one of the most common landscapes on the surfaces of continental ice sheets

39 and mountain glaciers, is formed by the incision and erosion effects of glacial meltwater, which has been shown to have river

40 morphology and processes similar to those of terrestrially based bedrock rivers (Knighton, 1981; Pitcher and Smith, 2019)

41 with the discharge closely related to the channel geometry (e.g., width and depth) (Jarosch and Gudmundsson, 2012). However,

42 compared with the relatively sophisticated methods for estimating terrestrial river runoff by retrieving the water level, river

43 width, channel slope, and flow velocity from satellite remote sensing data (Bjerklie et al., 2018; Xu et al., 2024), the retrieval

44 methods for meltwater runoff of mountain glaciers remain less developed, mainly for two reasons. First, most supraglacial

45 rivers of mountain glaciers are very narrow (sub-meter or meter scale), making it difficult to be identified from the commonly

46 used satellite images with meters or tens of meters pixel sizes, even though these satellite images have been widely used to

47 extract the spatial distribution of relatively wider supraglacial rivers on the Greenland Ice Sheet (GrIS) and other large polar

48 glaciers (e.g., Bell et al., 2017; Legleiter et al., 2014; Yang and Smith, 2016; Zhang et al., 2023). Second, it remains challenging

49 to obtain continuous field measurements or estimations of supraglacial river discharge from those ice sheets or mountain

50 glaciers under relatively harsh environmental and climatic conditions (Gleason et al., 2016). To date, estimates of meltwater

51 runoff at basin or larger scales have often relied either on the limited field observations (Gleason et al., 2016; Smith et al.,

52 2017, 2021) or on glacier runoff models driven by coarse-resolution climate data (Beamer et al., 2016; Hock, 2005; Sicart et

53 al., 2008; Wang et al., 2024; Yang et al., 2025). Although in situ meteorological observations from weather stations are used

54 in some glacier studies, such data are often unavailable or sparse for remote glacierized regions, leading to uncertainties in

55 modeled runoff that hinder a robust quantitative analysis of its relationship with supraglacial channel geometry (Smith et al.,

56 2017). Furthermore, during the ablation season, supraglacial channels can terminate in meltwater lakes, moulins, and crevasses

57 (Colgan et al., 2011; Smith et al., 2015; Yang and Smith, 2016), further complicating the estimation of meltwater runoff of

58 supraglacial rivers.

59 Currently, uncrewed aerial vehicle (UAV) remote sensing has been widely used to monitor glacier changes by combining its

60 optical images and digital elevation model (DEM) data or airborne synthetic aperture radar (SAR) images, which are performed

61 at a centimeter-level spatial resolution (Bhardwaj et al., 2016; Dall'Asta et al., 2017; Hugenholtz et al., 2013; Immerzeel et al.,

62 2014; Kraaijenbrink and Immerzeel, 2025; Śledź et al., 2021; Wang et al., 2025). Although UAVs are generally equipped with

63 visible light cameras, which have limited ability to discriminate water bodies from the surrounding narrow and deep

64 supraglacial channels on mountain glaciers, UAV remote sensing data have great strengths in identifying supraglacial channel

65 networks and their cross-sectional geometry. According to studies based on UAV field observations, channel migration and

66 curvature adjustments occur annually in supraglacial rivers in polar glaciers (Bergstrom et al., 2021; Rippin et al., 2015; St

67 Germain and Moorman, 2019). Similarly, significant interannual variability in supraglacial rivers has also been reported in the
68 Ganglongjiama Glacier on the central Tibetan Plateau using a terrestrial laser scanner (TLS) data (Xue et al., 2024). Our field
69 observations at the Qiyi Glacier also revealed that supraglacial channel adjustment appears to be positively related to the
70 intensity of ice melting on an annual timescale: years of more intense melting are generally characterized by stronger surface
71 meltwater erosion with deeper and wider channels, and vice versa. This phenomenon inspired us to investigate the relationship
72 between the channel morphology and annual discharge of supraglacial rivers. Therefore, in this study, using a DJI M300 series
73 UAV, a 5 cm spatial resolution DEM and orthomosaic map over the Qiyi Glacier were obtained to extract the channel
74 geometric parameters at different elevations, which were used to explore their relationships with meltwater discharge
75 calculated by field observations rather than the glacier runoff model.

76 **2 Data and methods**

77 **2.1 Study area**

78 The Qiyi Glacier, located in the Qilian Mountains (39°14′13″N, 97°45′18″E), is a typical polythermal mountain glacier of the
79 Tibetan Plateau (Fig. 1). The elevation of the Qiyi Glacier ranges from 4,322 to 5,158 m.a.s.l., with a total area of approximately
80 2.69 km^2 and length of 2.9 km in 2023. Since 1975, the glacier area has shrunk by approximately 4.5%, with the terminus
81 continuously receding by 235 m. Mountain glaciers (including the Qiyi Glacier) offer important water resources to the
82 downstream arid regions over the Hexi Corridor, with glacier meltwater accounting for approximately 20% of the runoff of
83 the Beida River (Wang et al., 2017). We have undertaken regular meteorological, hydrological, and mass balance observations
84 on Qiyi Glacier from June to August since 2002, which have demonstrated an increase in melt, particularly since 2016
85 According to our regular meteorological, hydrological, and mass balance observations (June to August) starting in 2002, the
86 Qiyi Glacier has suffered from an obviously increasing ice melting trend since 2016 (Chen et al., 2024). Over the past decade,
87 the acceleration of glacial melting has increased surface meltwater runoff, which has contributed to the deepening and widening
88 of supraglacial stream channels.
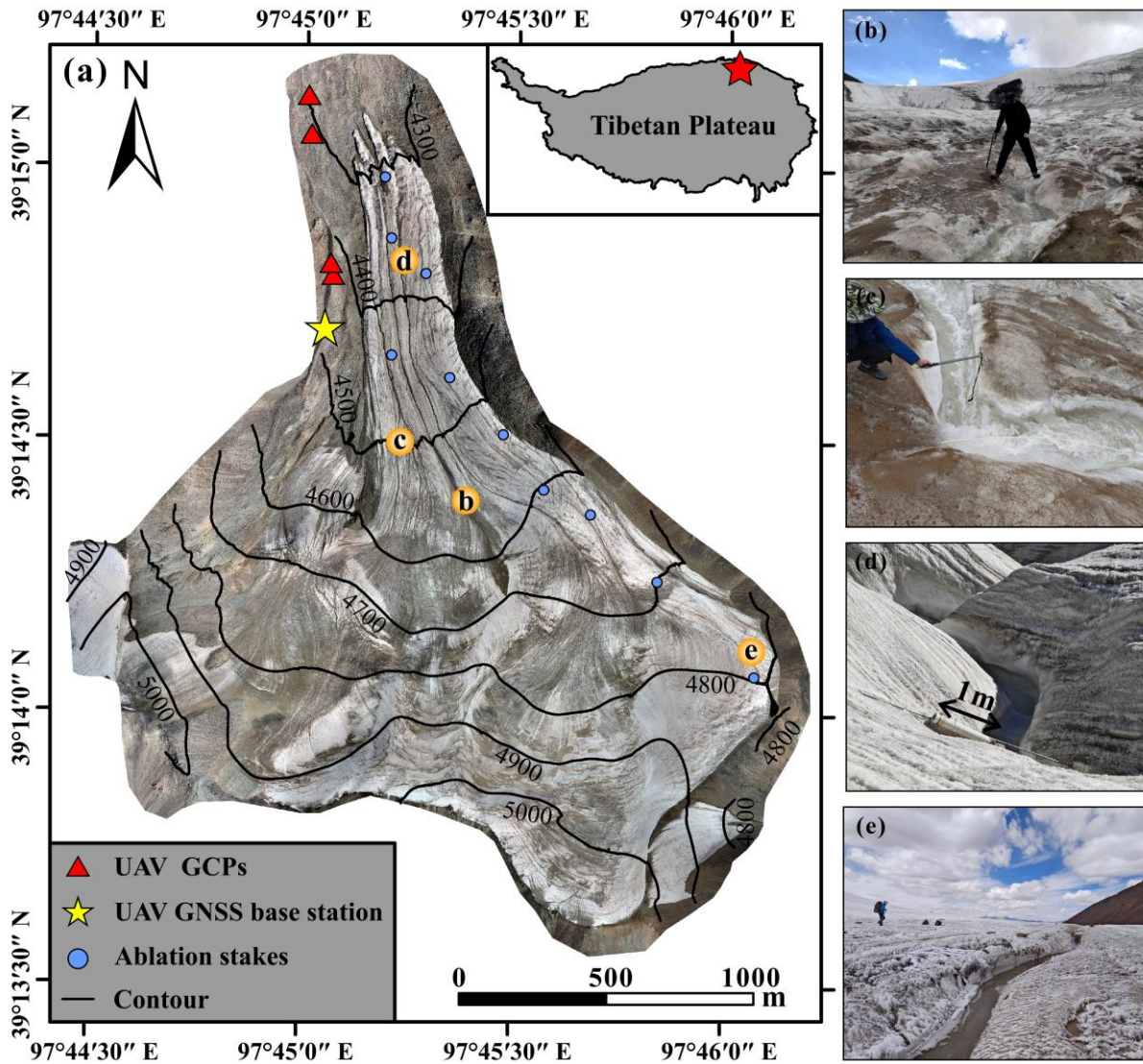
Figure 1. Location of the Qiyi Glacier and photos of its typical supraglacial stream channels. (a) Orthomosaic map of the Qiyi Glacier generated from UAV data (5 cm spatial resolution), with red triangles marking the locations of ground control points (GCPs) each with a fixed solution for UAV flights, yellow stars indicating the Global Navigation Satellite System (GNSS) base station of UAV, blue dots representing the locations of ablation stakes on the glacier, and orange circles showing the locations where photos (b)–(e) were taken.

2.2 UAV data acquisition and processing

A DJI Matrice300 real time kinematic (RTK) UAV was used to produce the DEM and orthophotos (both with a resolution of 5 cm) of the Qiyi Glacier. The UAV was equipped with a Zenmuse L1 lens integrating a visible-light camera and a light detection and ranging (LiDAR) sensor. From August 15 to August 20, 2023, 2,585 photographs and LiDAR data were collected

98   at a flight altitude of 100 m to cover the entire Qiyi Glacier. The geolocation accuracy requirements of the DEM and

99   orthomosaic map were ensured by ground control points (GCPs), and Hi-Target RTK was used to obtain fixed solutions for

100 high-precision geolocation information.

101 Pix4D Mapper 4.5.6 software was used to process the visible light images, including data preprocessing, aerial triangulation,

102 and point cloud encryption. The root mean square errors (RMSE) in x, y, and z directions for the positions of the GCPs were

103 0.24m, 0.09m, and 0.35m, respectively. The LiDAR data were processed using the CloudCompare and Lidar360 software,

104 including denoising, smoothing, thinning, and rasterizing the point cloud. It should be noted it is relatively difficult to

105 identify homologous image points on the snow surface of the upper glacier under visible light, and the density of the point

106 cloud data generated from visible light images is very low, while for the photons actively emitted by the lidar sensor, due to

107 their property of being easily absorbed by the liquid water, the density of the point cloud is very low in the region of the lower

108 glacier where the melting is strong. Therefore, these two types of point-cloud data have good spatial complementarity for

109 generating a complete high-precision point-cloud dataset for glacier surfaces. The iterative closest point (ICP) algorithm was

110 applied to register these two, and the merged point-cloud data were rasterized to the final DEM with a spatial resolution of

111 0.05 m.

2.3 Extraction of morphological characteristics of supraglacial channels

113 The supraglacial channel network was extracted from UAV-derived DEM data by using the hydrological analysis module of

114 the ArcGIS platform and Global Mapper software, from which we extracted several morphological characteristics, including

115 channel sinuosity (SIN), lateral deviation (LD), channel gradient (G), and cross-section geometry (width W, depth Δh, and

116 width/depth ratio) (Fig. 2). To ensure consistency in defining channel geometry, we applied a standardized approach to

117 determine channel width and depth. Since supraglacial channels are continuously eroded by rapid water flow, there are

118 relatively distinct inflection points in the slope of the cross-section. The two points on the cross-section with the steepest slope

119 gradients were designated as h_1 and h_2. Channel depth (Δh) was defined as the average vertical distance from these two points

120 to the lowest point of the channel, whereas channel width (W) was defined as the horizontal distance between h_1 and h_2. A

121 representative cross-section (channel A at 4350 m) has been included in the Supplement (Fig. S1) to illustrate the positions of

122 h_1 and h_2.

123 Supraglacial rivers can terminate in crevasses and moulins, potentially leading to the misidentification of channels. Although

124 crevasses also exist in the Qiyi Glacier, they are generally small in size and mainly distributed in the steep area of the upper

125 glacier as well as the edge area of the middle and lower parts; therefore, they have a minor influence on the process of river

126 confluence and continuity of the river channel (Fig. 1). After several comparative trials, a minimum drainage area of 0.02 km^2

127 was determined as the threshold for the automatic extraction method. The automated algorithm identified a total of 33 channel

128 segments, including not only the six main channels (labeled A–F in Fig. 4a) but also smaller, low-order tributaries. To ensure

129 the realism of the extracted channels, all automatically derived streams were carefully compared with the orthophotos, channels

130 that could not be clearly identified in the orthophotos were truncated, particularly small tributaries and river sections at the

131   upstream headwaters. Finally, six main supraglacial channels on the Qiyi Glacier were correctly identified and extracted, from

132   which the glacier was divided into six catchments (Fig. 4a).

133
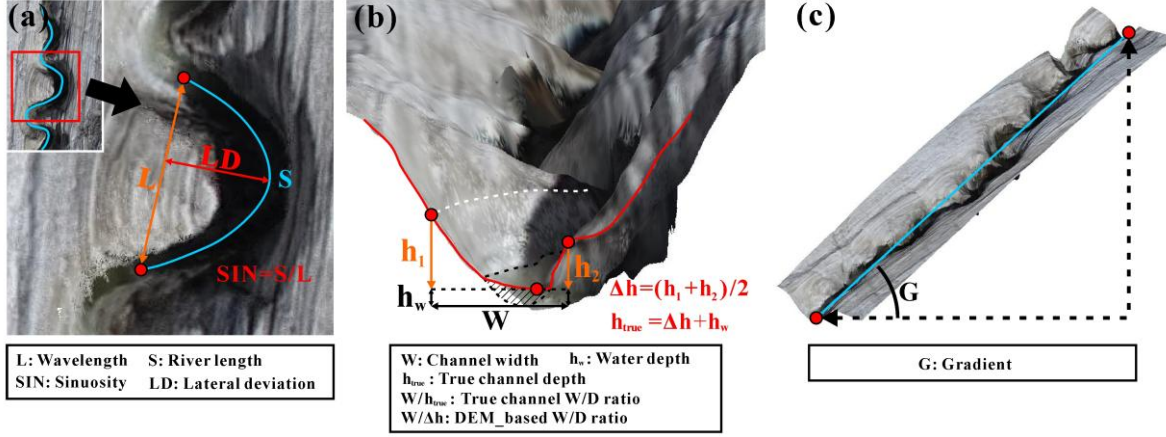
134   **Figure 2.** Diagrams showing the process of obtaining the channel geometric parameters: (a) sinuosity and lateral deviation of an individual

135   meander; (b) geometry of the channel profile (width, depth, and width/depth ratio); the white dashed line indicates the maximum slope, and

136   the black dashed line and shaded area indicate the water surface and underwater channel profile, respectively; (c) the channel gradient.

2.4 Calculation of the annual glacial discharge transported by supraglacial channels

138   Excluding the negligible glacier mass loss due to surface sublimation, the annual meltwater yield of a given pixel (5 cm × 5

139   cm) on the glacier can be estimated as follows:

140      $Q_a = (P_0 - MB + (H - 4310) \times 6.8/100) \times S,$ (1)

141   where P_0 is the precipitation at the glacier terminus based on field observations, MB and H represent the glacier mass balance

142   and the elevation of the pixel, mass balance is expressed in millimeters water equivalent (mm w.e.), with negative values

143   indicating mass loss. 4,310 (m) means the elevation of the glacier terminus, S denotes the area of the pixel, and 6.8 mm/(100m)

144   is the precipitation gradient regressed from rain gauge networks on the Qiyi Glacier (Jiang et al., 2010).

145   From the nine ablation stakes across the glacier with long-term mass balance (MB) measurements, the MB of all pixels was

146   calculated using spatial extrapolation (Fig. 3a). The stakes were measured at annual intervals. Several new ablation stakes were

147   installed on July 20, 2022, and subsequently measured and maintained on August 24, 2023. Detailed information for each

148   stake data, including stake ID, position, elevation, and mass balance records, are provided in Supplement (Table ~~S2~~S1). The

149   uncertainty of the mass balance based on the ablation stakes is discussed in detail in Section 4.2.

150   Because our rain gauge observations at the glacier terminus were not collected every year, precipitation data from a neighboring

151   weather station (Tuole Station, ~70 km from the Qiyi Glacier) were used to establish a relationship to reconstruct the

152   precipitation at the glacier terminus. Comparisons between two sets of precipitation data during the period 2006–2013 (Fig.

153   3b) showed a good linear relationship, with the coefficient of determination (R^2) value as high as 0.967; therefore, the annual

154 precipitation (P_0) of 2023 at the glacier terminus (4,310 m) can be inferred from the precipitation data at the Tuole station (P_t)

155 as follows:

156 $$P_0 = 1.1267 \times P_t + 15.205. \tag{2}$$

157 Equations 1 and 2 were used to calculate the meltwater yield for each pixel. From the upper to the lower glacier, the volume

158 of discharge transported by the ice channel at each 10 m elevation decrease can be determined from watershed analysis by

159 placing outlets at each elevation interval (10 m).
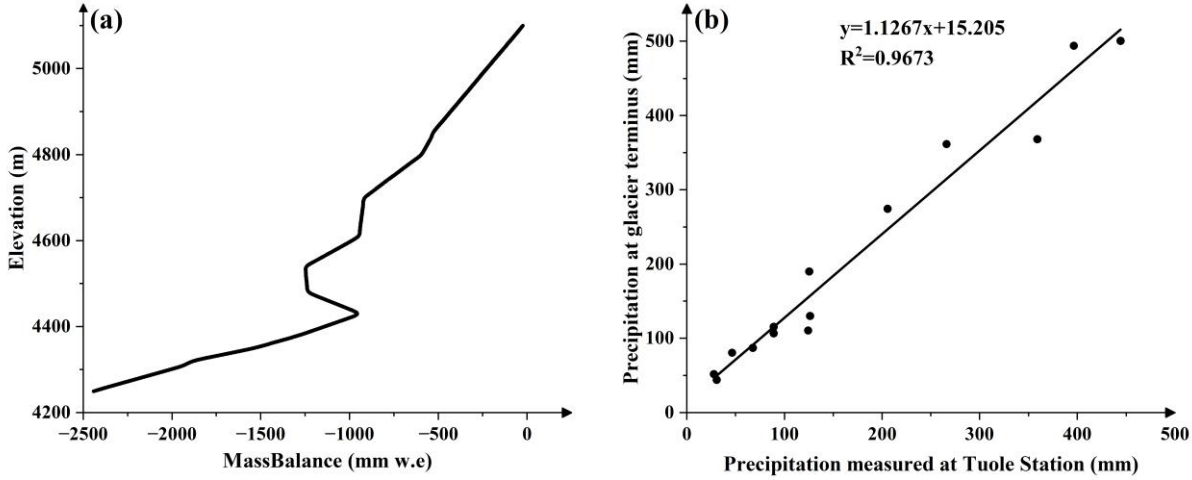
160

161 **Figure 3.** (a) Variations in mass balance of the Qiyi Glacier reconstructed from ablation stake measurements with elevation in 2023. (b)

162 Comparisons of monthly/annual precipitation between Tuole station records and rain gauge observations at the terminus of Qiyi Glacier

163 during 2006–2013.

164 **2.5 Statistical modeling methods**

165 Pearson's correlation (r) and Spearman's rank correlation (ρ) were used to analyze the correlation between the morphological

166 characteristics of the supraglacial channels and the annual meltwater discharge transported by these channels at different

167 elevations. Because previous studies found that the total energy of the flowing water (including pressure energy, gravitational

168 potential energy, and kinetic energy) is the initial driving force for the channel formation (Rodríguez–Iturbe et al., 1992) and

169 that discharge and slope are the most influential fluvial factors (St Germain and Moorman, 2019), here we took the product of

170 gradient G and annual discharge Q_a as the water potential energy factor GQ_a in the correlation analysis.

171 In addition to the water flow conditions (discharge and water potential energy), the morphology of supraglacial channels is

172 influenced by other factors, such as pre-existing ice structure (e.g. fractures and moulins), thermal differences (ice and water

173 temperatures and channel frictional heat), topographic relief (slope, roughness, and surface albedo), and ice velocity (Pitcher

174 and Smith, 2019). To eliminate the influence of discharge and water potential energy, Q_a and GQ_a were used as control

175 variables to conduct a partial correlation analysis for each pair of morphological characteristics.

176 The fitting model was developed using only morphological characteristics that showed a strong correlation with the discharge,

177 and the regression methods included simple linear regression, stepwise regression, and nonlinear least squares (NLS). The

178 coefficient of determination (R^2), root mean square error (RMSE), mean absolute error (MAE), and normalized root mean

179 square error (nRMSE) evaluated the performance of the fitting models. Specific details of the regression model and error

180 analysis can be found in Sections 3.4 and 4.2.

3 Results

3.1 Supraglacial channel network and annual discharge

183 The watersheds of the six main supraglacial channels covered 92.02% of the total area of the Qiyi Glacier (Fig. 4a) with an

184 annual discharge volume of about 2.4×10^6 m^3 (each ranging from $0.07–0.66 \times 10^6$ m^3), which contributed 89.43% to the total

185 meltwater of the glacier surface (2.68×10^6 m^3) during the hydrological year from August 2022 to August 2023. Approximately

186 63.21% of the channel discharge was transported to the glacial terminus (by channels A, B, C, and D). In particular, the

187 discharge in the lower reaches of channels A and C was significantly higher than that in the other channels (Fig. 4b), accounting

188 for approximately 45.30% of the total glacial discharge. Channel F was the only river that was newly formed during the

189 summer of 2023 because two separate smaller catchments merged into one larger catchment, reflecting how supraglacial rivers

190 reshape the surface topography in a short period as meltwater flow increases.
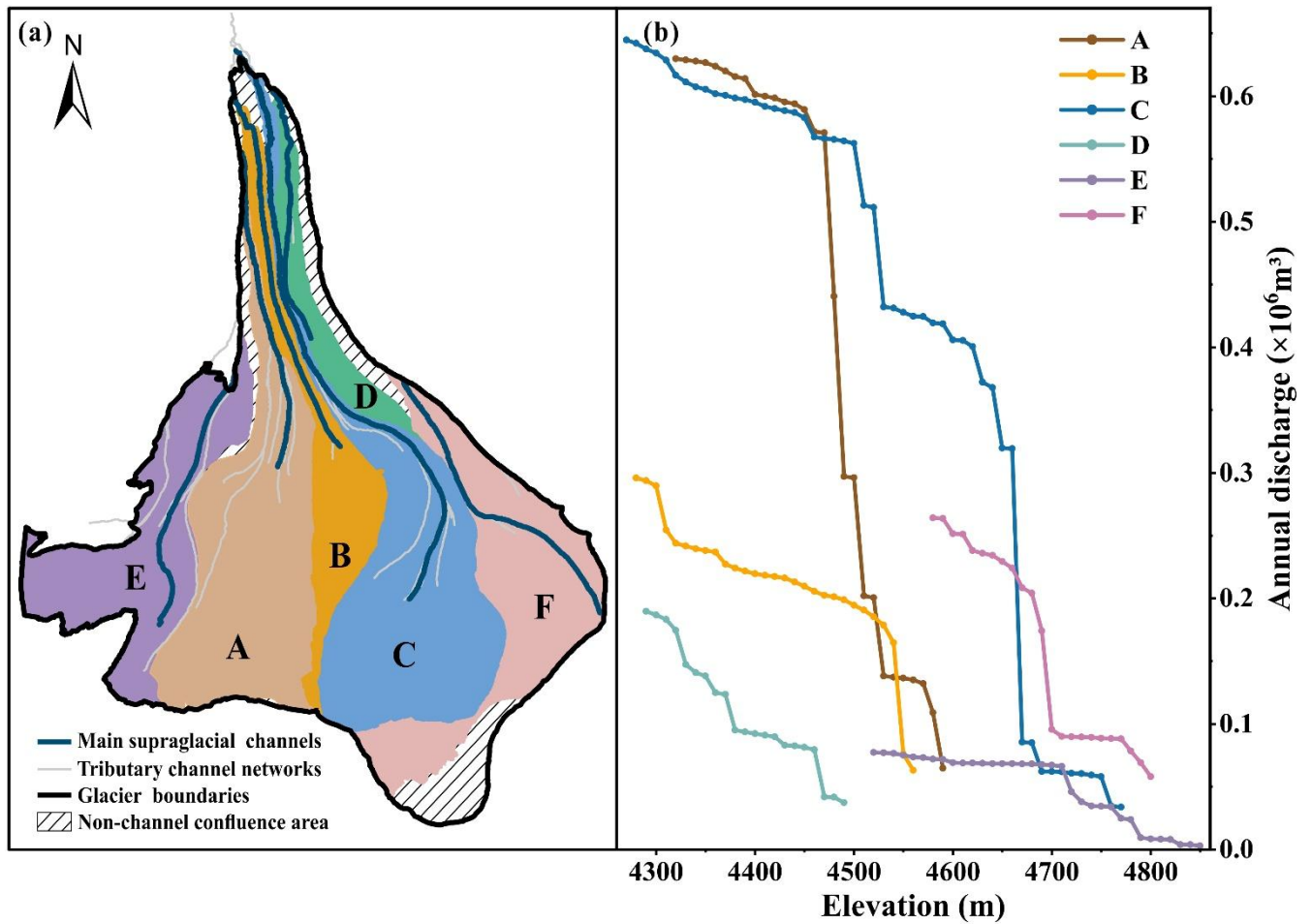
Figure 4. (a) Supraglacial channel network over the Qiyi Glacier and (b) variations in the annual discharge of six main supraglacial channels with elevation changes at a 10 m elevation interval. The catchment areas of the main channels are filled with different colors.

3.2 Spatial variability of morphological characteristics of supraglacial channels

3.2.1 Variations in the sinuosity and lateral deviation

The mean sinuosity and mean lateral deviation integrated with a 10 m elevation interval show similar variation trends among the six main supraglacial channels, and both are lower in the upper reaches and higher in the lower reaches (Fig. 5a and 5b). The median of 10 m average sinuosity and lateral deviation ranges from 1.05 to 1.27 and 0.42 to 1.06, respectively. The maximum sinuosity and lateral deviation were observed near the outfalls of channels C (2.75) and D (4.41), respectively. In general, channels with relatively higher discharge (channels A and C) tended to have larger sinuosity and lateral deviation in both their median and mean, while those with relatively lower discharge (e.g., channels D and E) had lower sinuosity and

202 lateral deviation (Fig. 5c), suggesting a possible positive correlation between the discharge and sinuosity/lateral deviation of
203 the supraglacial channel.
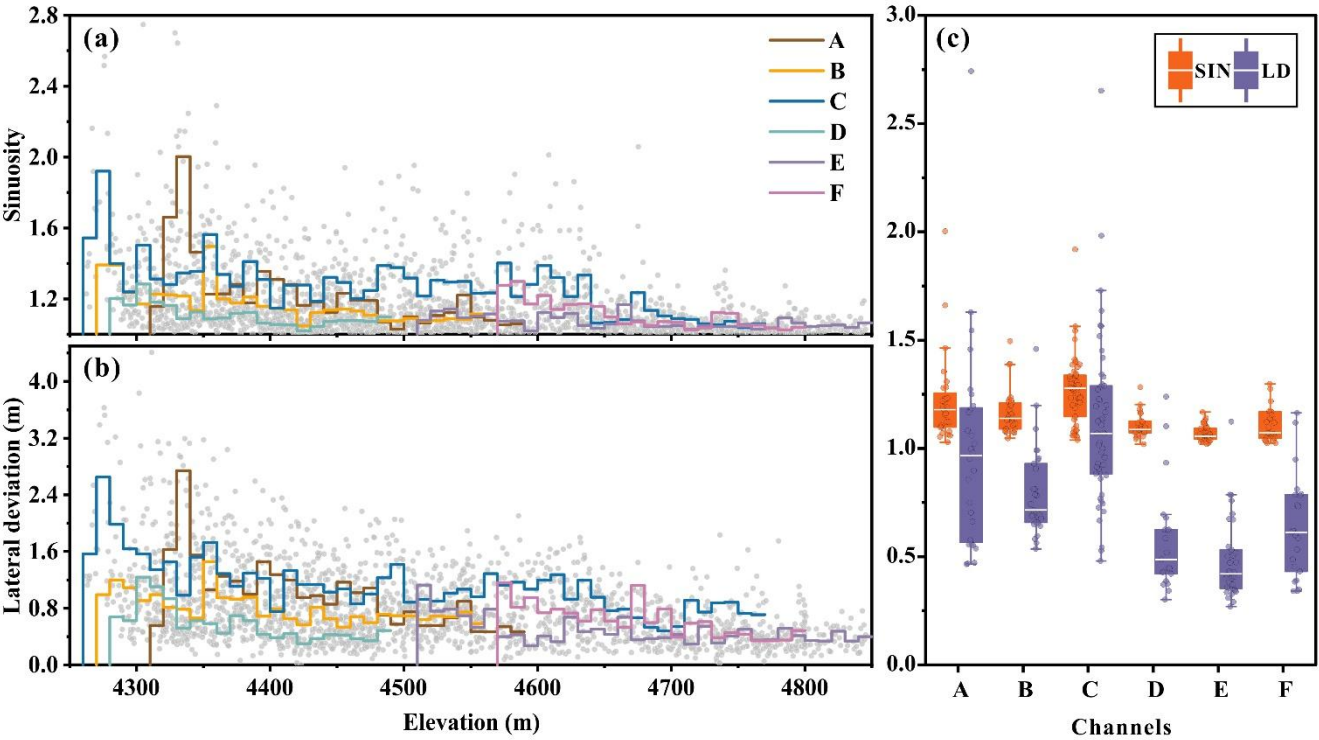
Figure 5. Variations in the (a) sinuosity and (b) lateral deviation of six supraglacial channels (gray dots indicate values at each meandering)
and their mean at a 10 m elevation interval (colored stairs); (c) box plot of 10 m average sinuosity and lateral deviation for six supraglacial
channels, where the box represents the interquartile range (IQR), the whiskers denote 1.5 times the IQR from both ends of the box, and the
white horizontal line shows the median; the labeling A to F corresponds to channels A to F as shown in Fig.4a.

3.2.2 Variations in the channel gradient

The incision depth (no more than 1 m) of supraglacial rivers is much shallower than the ice thickness of the Qiyi Glacier (tens
to hundreds of meters), which implies that their incision ability is relatively limited. Changes in the gradients of the six
supraglacial channels showed a relatively consistent pattern because they were influenced by the complex undulating
topography of the glacier surface (Fig. 6). The mean gradient of the six supraglacial channels ranges from 0.22 to 0.41, with
channel E having the steepest mean gradient. For a 10 m elevation interval, the maximum channel gradient (0.81) was observed
at an elevation of 4,640 m in channel E, while the minimum channel gradient (0.09) was found in channel F near the glacier-
covered mountain pass.
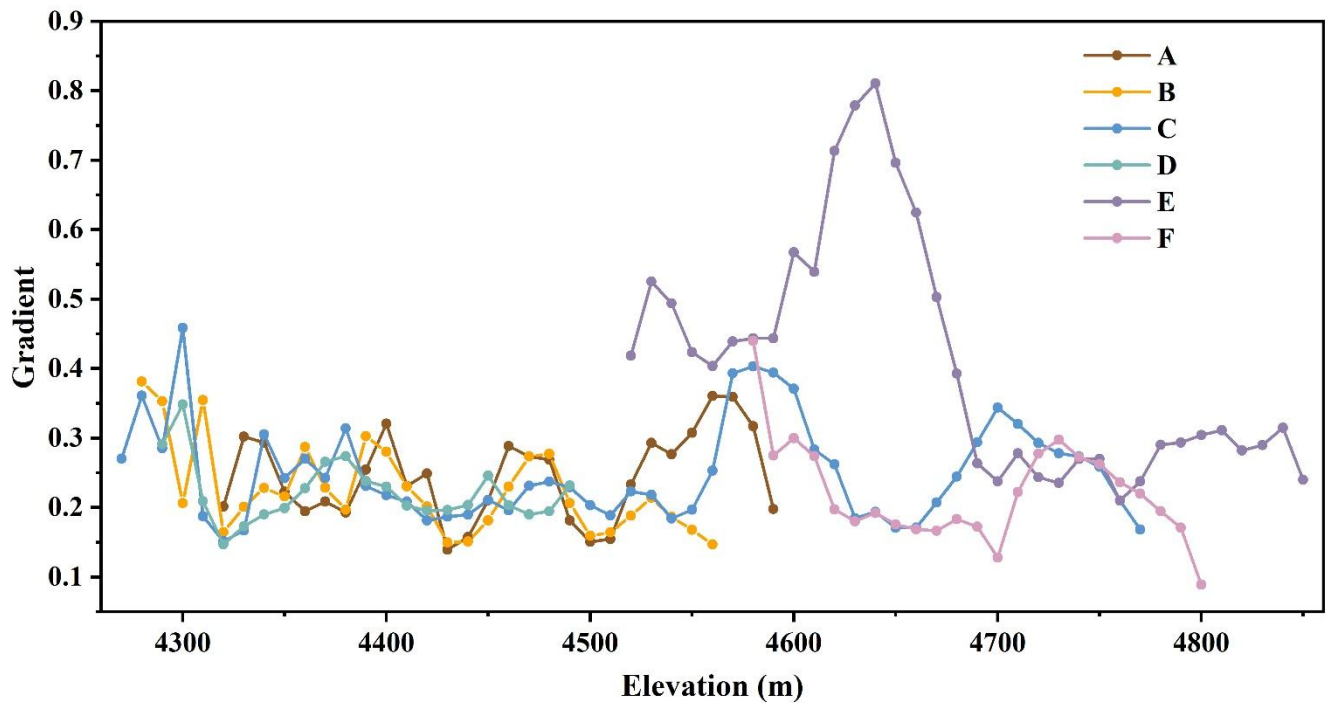
Figure 6. Variations in the gradient of six supraglacial channels with elevation at a 10 m interval (the labeling A to F corresponds to channels A to F as shown in Fig. 4a).

3.2.3 Variations in the geometry of the channel cross section

Both channel width and depth of all six supraglacial channels generally show decreasing trends with increasing elevation (Fig. 7a and 7b), with the maximum channel width and depth (1.25 and 1.00 m, respectively) observed near the channel outfall at the glacier terminus. In general, for a given channel, its width increases with depth and vice versa; however, exceptions are found for the lower reaches of channel C, which does not have the widest channel near the outlet with the deepest channel. Another noteworthy point is that, instead of the outlet, channel F has the deepest and relatively wider channel at its headwater at 4,800 m.a.s.l., possibly because its headwater is a shallow supraglacial lake over a relatively flat mountain pass that provides warmer meltwater to the channel.

Assuming a constant ratio of water depth to channel depth (water depth + Δh), the ratio of width to Δh was calculated as a surrogate for the true channel width/depth (W/D) ratio. In general, the W/D ratio increased with elevation for all channels, except the upper reaches of channel F, which may have been influenced by the supraglacial lake at the headwater (Fig. 7c). The distribution pattern of the W/D ratio with elevation suggests that regions with a larger discharge in the lower part of the glacier may experience stronger downward erosion than lateral erosion.

233
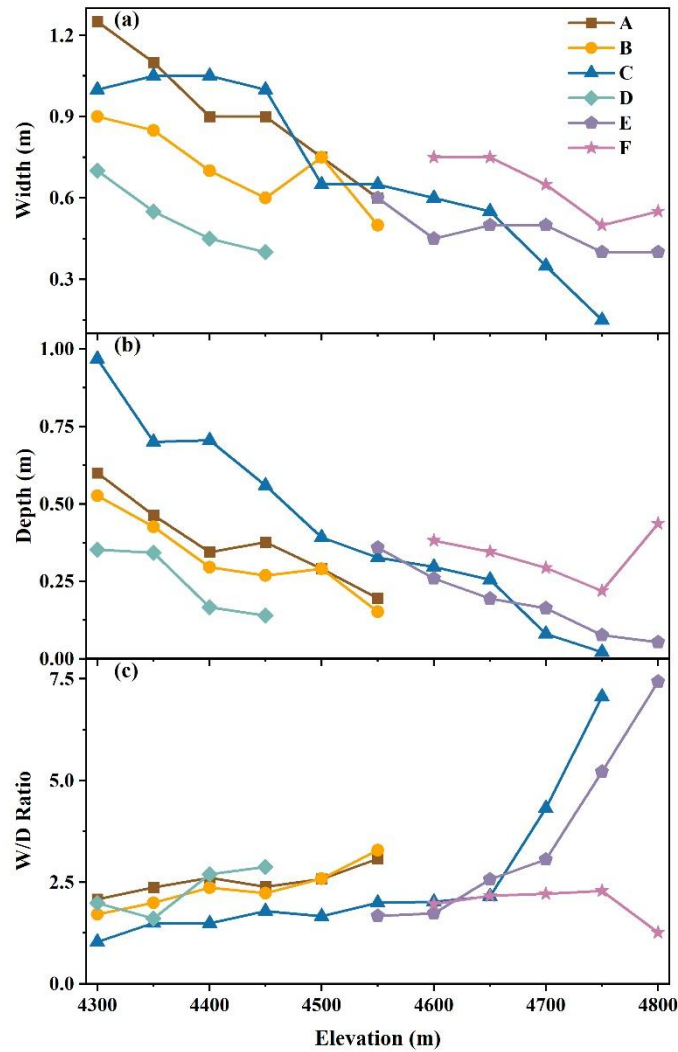
Figure 7. Variations in (a) width, (b) depth, and (c) *W/D* ratio of six supraglacial channels with elevation changes at a 50 m elevation interval.

3.3 Relationships between channel geometry and annual discharge

236 Both the Pearson and Spearman correlations showed that annual discharge (Q_a) was significantly positively correlated with
237 sinuosity, lateral deviation, channel width and depth, but significantly negatively correlated with width to depth ratio(W/D)
238 and gradient (Table 1). The water potential energy (GQ_a) showed a correlation pattern similar to that of discharge. Among all
239 the geometric parameters, channel width showed the strongest correlation with discharge in both Pearson ($r = 0.82$) and
240 Spearman ($\rho = 0.86$) correlation analyses, followed by lateral deviation ($r = 0.80$, $\rho = 0.82$), which was very similar to those
241 of water potential energy despite of some slight differences. This suggests that both the channel profile and the meander of

supraglacial channels were closely correlated with the discharge and water potential energy, and thus could be considered as indicators of changes in them.

Table 1. Pearson's (r) and Spearman's rank (ρ) coefficients of geometric parameters with discharge Q_a and water potential energy GQ_a, all coefficients that are significant at a minimum level of 0.05, 0.01, and 0.001 are labeled with *, **, and ***, respectively.

	Sinuosity		Lateral deviation		Width		Depth		W/D		Gradient	
	r	ρ	r	ρ	r	ρ	r	ρ	r	ρ	r	ρ
Q_a	0.73***	0.80***	0.80***	0.82***	0.82***	0.86***	0.74***	0.76***	-0.44***	-0.51***	-0.20**	-0.21**
GQ_a	0.77***	0.82***	0.81***	0.79***	0.76***	0.82***	0.74***	0.74***	-0.43***	-0.53***	0.15*	0.10

Partial correlation analysis, after excluding the effects of discharge and water potential energy, further revealed an inherent connection between the geometric parameters (Table 2). When discharge was considered the control variable, the highest correlation coefficient was found between sinuosity and lateral deviation (0.75), followed by that between width and depth (0.70). When water potential energy was used as the control variable, the highest correlation was observed between width and depth (0.72), as well as between sinuosity and lateral deviation (0.72). Regardless of whether discharge or water potential energy was used as the controlling factor, after removing their influence, strong correlations remained between sinuosity and lateral deviation, width and depth, indicating that both channel meander and profile characteristics exhibited stable internal variation patterns. Furthermore, the relatively weak correlation between channel meander characteristics and width or depth showed that their variations may not be synergistic, and thus can be jointly used to estimate discharge. These findings provided a crucial reference for the selection of independent variables in discharge regression models.

Table 2. The partial correlation coefficient between each two geometric parameters, with discharge Q_a and water potential energy GQ_a as control variables. Significance levels of 0.05, 0.01, and 0.001 are denoted by *, **, and ***, respectively.

	Sinuosity		Lateral deviation		Width		Depth		W/D	
	Q_a	GQ_a	Q_a	GQ_a	Q_a	GQ_a	Q_a	GQ_a	Q_a	GQ_a
Lateral deviation	0.75***	0.72***								
Width	0.18*	0.20**	0.09	0.16*						
Depth	0.29***	0.24**	0.26***	0.24***	0.70***	0.72***				
W/D	-0.07	-0.05	0.04	0.05	-0.47***	-0.46***	-0.53***	-0.53***		
Gradient	0.20**	-0.14	0.13	-0.28***	0.13	-0.27***	0.29***	-0.08	-0.24**	-0.07

3.4 Regression models of annual discharge of the supraglacial channels

As stated in Section 2.5, both linear and nonlinear regression models were used to fit the annual discharge Q_a of the supraglacial channels using geometric parameters with significant correlations with Q_a. For the linear regression method, all variables were initially included to obtain an optimal fit of Q_a; then, a stepwise regression method was used to establish a more efficient linear fitting formula by excluding variables with minimal impact on the regression results. For the nonlinear regression method, the focus was on the robustness of the NLS model, which was fitted using a minimal number of parameters that are easier to obtain without significantly reducing the simulation results.

As illustrated in Fig. 8a, the linear regression model incorporating all variables (*SIN*, *LD*, *G*, *W*, *D*, β, and Elevation) showed a similar R^2 value to that of the stepwise regression model including only *LD*, *G*, and *W* (0.780 vs. 0.782), with RMSE of 0.096 and 0.097×10^6 m^3, MAE of 0.077 and 0.076×10^6 m^3, and nRMSE of 10.64% and 10.60%, respectively. This indicates that the inclusion of Elevation, *D*, and β in the linear regression model does not improve the explanation of the variation in the annual discharge. The stepwise regression model was expressed as follows:

$$Q_{step} = 0.230 \times LD - 0.232 \times G + 0.493 \times W - 0.181. \tag{3}$$

In contrast to the difficulty in obtaining width *W* in Eq. (3) from high-spatial-resolution satellite images, *LD* and *SIN* are the most easily and accurately extracted supraglacial channel characteristics from the digitized river network. According to the correlation analysis described in Section 3.3, the *r* values of *LD* and *SIN* with GQ_a were both improved compared with those of Q_a, particularly for *LD*, which showed the highest *r* value with GQ_a. Therefore, it may be more appropriate to develop a regression model using a nonlinear relationship. *LD* was selected as the independent variable using a simple linear regression model.

$$GQ_a = a \times LD + b, \tag{4}$$

where *a* and *b* are the regression coefficients. The nonlinear equation can be obtained by transforming Eq. (4) as follows:

$$Q_{NLS} = a \times \frac{LD}{G} + \frac{b}{G} + c, \tag{5}$$

where the regression coefficients are $a = 0.108$, $b = -0.061$, and $c = 0.137$ in our study area and Q_{NLS} is the annual discharge predicted using the nonlinear model. The R^2, RMSE, MAE, and nRMSE values in Eq. (5) are 0.662, 0.122×10^6 m^3, 0.091×10^6 m^3, and 12.87%, respectively.

When compared with the observed annual discharge, both the linear and nonlinear models exhibited large fluctuations. Therefore, the stepwise and NLS methods were smoothed using a five-point moving average, and the filtered results were more consistent than the original curves, with R^2 increasing to 0.818 and 0.814, respectively. Their RMSE, MAE, and nRMSE values were 0.091 and 0.099×10^6 m^3, 0.073 and 0.077×10^6 m^3, and 12.58% and 15.11%, respectively. The NLS model is more robust and can be more widely applied as its input parameters require only *LD* and the channel gradient *G*, which can be easily calculated from the DEM data.
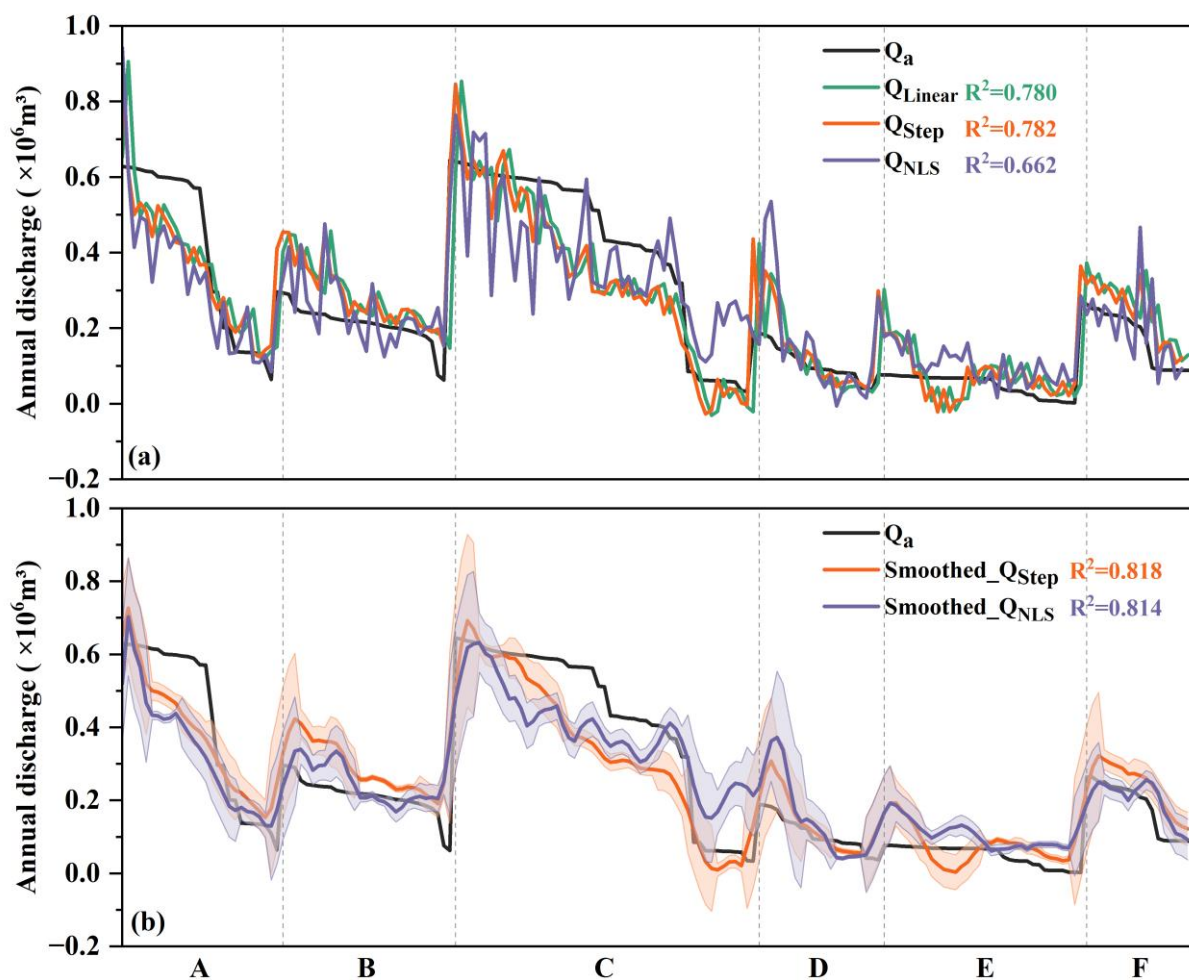
Figure 8. Comparison between observed annual discharge (Q_a) and (a) original results and (b) five-point moving average fitted results using linear, stepwise, and NLS regression models. The shaded error bands indicate twice the standard deviation range. The x axis is arranged at an order of increasing elevation for each channel meander, and each channel is divided by vertical gray dashed lines.

4 Discussion

Smith et al. (2015) highlighted that the processes of meltwater generation, storage and transport on the surface of the Greenland Ice Sheet "remain one of the least studied hydrological processes on Earth". This knowledge gap is also significant for mountain glaciers. The extreme lack of field observations and challenges associated with data collection have resulted in significant uncertainties in our understanding and estimation of meltwater discharge volume from mountain glaciers, particularly in the Tibetan Plateau region. Previous studies have primarily estimated supraglacial runoff through direct discharge observations or runoff models driven by meteorological data (Muthyala et al., 2022; Yang et al., 2019). Yang and Smith (2016) demonstrated

302 that catchment area is a dominant control on runoff, with larger basins generally producing greater discharge. However, when

303 catchments originate from high elevation mountain glaciers, steep and complex glacier surfaces may weaken the dominant

304 relationship between catchment area and glacier runoff. The supraglacial channel morphology is more strongly influenced by

305 local topography, which is one of the reasons we retained gradient as a variable. Building on established physical principles,

306 given the significant correlations of Q_a and GQ_a with the geometric parameters of the supraglacial channels (Table 1, 2 and

307 Fig. 8a, 8b), we innovatively used these geometric parameters to predict the surface meltwater discharge in mountain glacier

308 and establish quantitative relationship between supraglacial channel geometry and annual glacier runoff. Our results are ~~of~~

309 ~~great importance~~significant for estimating meltwater discharge over mountain glaciers with complex topography. In the

310 following sections, we will further discuss the uncertainties of the supraglacial channel parameters, limitations of the regression

311 models, and the applicability of these models.

4.1 Uncertainties in supraglacial channel parameters

313 The sinuosity and lateral deviation of supraglacial channels can be derived from DEM data based on hydrological analysis or

314 digitization of the orthomosaic map (Fig. 2a). If the spatial resolution requirements of visible-light images are satisfied, the

315 sinuosity and lateral deviation are the easiest parameters to obtain. However, the identification of other parameters such as

316 river width, depth and gradient requires DEM data with a higher spatial resolution (Fig. 2b). While the width is discernible in

317 certain regions from visible light images (e.g., the wider parts of the river at the lower reaches of the glacier), discriminating

318 the spectral character between the narrower channel and the adjacent bank over the upper and middle parts of the glacier

319 remains a challenge, making it difficult to extract complete width data across the entire glacier based on the visible light image

320 alone.

321 In addition, during the glacial ablation season, part of the supraglacial river channel is often occupied by flowing water, making

322 it difficult to derive the true channel depth from UAV-based DEM data. Therefore, the UAV-based depth (Δh) represents the

323 channel depth by considering the water surface as the "bottom" of the glacier (Fig. 2b). This might exert a greater influence in

324 the shallower channel over the upper glacier but a relatively minor influence for the deeper channel over the lower parts. This

325 study assumes a constant ratio of true channel depth to depth above the water surface (i.e., Δh), although this assumption

326 inevitably introduces some error when compared to actual conditions. Furthermore, the channel depth was not included in the

327 stepwise regression model, but this does not necessarily mean that the true channel depth cannot improve the predictive ability

328 of the regression model. Nevertheless, the depth of the supraglacial channel depends on centimeter-level DEM data, which

329 remains a challenge given the current development trend of high-resolution commercial optical satellites.

330 The channel gradient must also be derived from DEM data. In regions without UAV data, deriving the channel gradient ~~derived~~

331 from lower -resolution DEMs (e.g., 30 m GDEM, SRTM) ~~still~~ requires careful~~further~~ evaluation. Therefore, sinuosity and

332 lateral deviation are currently the most promising and accurate supraglacial channel parameters that can be obtained using

333 commercial optical satellite imagery at ~~a~~ centimetre~~centimeter~~ scale resolution.

4.2 Uncertainties in the calculation of glacier annual discharge and regression model

The reliability of glacier discharge calculations depends heavily on the accuracy of the observed glacier mass balance and precipitation data. The estimation of the distributed glacier mass balance is hampered by a lack of true validation values, which complicates the error assessment of spatial patterns in mass balance calculations based on single-point measurements of ablation stakes (Kaser et al., 2006; Xu et al., 2019). Specifically, the uncertainties of stake-based mass balance can be classified into three groups: (1) errors in field observations; (2) errors related to spatial extrapolation over the entire glacier; and (3) error due to unaccounted interannual changes in glacier area (Dyurgerov et al., 2002). Among these, (1) is very small (centimeter scale) and negligible at the annual scale, and (3) typically arises in multi-year studies. Since this study focuses solely on Qiyi Glacier's 2023 data, it is also excluded. The primary error is spatial extrapolation from ablation stakes, which typically requires higher resolution DEMs (e.g., obtained by TLS laser scanning (Xue et al., 2024)) for assessment, but such data were unavailable for Qiyi Glacier in 2022–2023 due to the absence of the UAV-derived high-resolution DEM in 2022. However, given the geographic proximity, similar glacier types, and comparable elevation range covered by stakes, we adopted the error assessment from Urumqi Glacier No.1 reported by Xu et al. (2019) as a reference, where the error of traditional stake-based mass balance was about ±0.12 m w.e., within 17%.

Regarding the error in the precipitation pattern over mountain glaciers, although the elevation effect of precipitation is obtained from in situ precipitation observations, the influence of wind and local topography also introduces some uncertainty in the precipitation distribution. To evaluate the combined effect of uncertainties in mass balance and precipitation on glacier discharge calculations, the meltwater volume of each pixel of the Qiyi Glacier was manually changed by a range of ±5%, ±10%, and ±20% for both stepwise regression and NLS model results. Based on the reference from Xu et al. (2019), we set the maximum uncertainty range of our stake-based mass balance estimates at ±20%. Under the maximum uncertainty scenario (20%), when compared with the original models without additional errors, ~~The error distribution of the fitting results showed that~~ the mean absolute error (MAE) for both stepwise and NLS methods remained very small ~~approached zero~~ (0.092 and 0.109×10^6 m³). ~~under different error scenarios,~~ The RMSE increased slightly from 0.097 and 0.122×10^6 m³ to 0.117 and 0.146×10^6 m³, while the nRMSE rose from 10.60% and 12.87% to 19.68% and 17.06% (Fig. 9), ~~RMSE fluctuated in the range of 0.077–0.146 × 10⁶ m³, and nRMSE ranged from 17.06% to 19.68% (Fig. 9), suggesting~~ showing reasonable robustness of the two current regression methods. These results indicate that~~,~~ although spatial extrapolation uncertainty is the dominant error source, it does not affect our finding that channel geometry can be used to estimate glacier runoff.

362
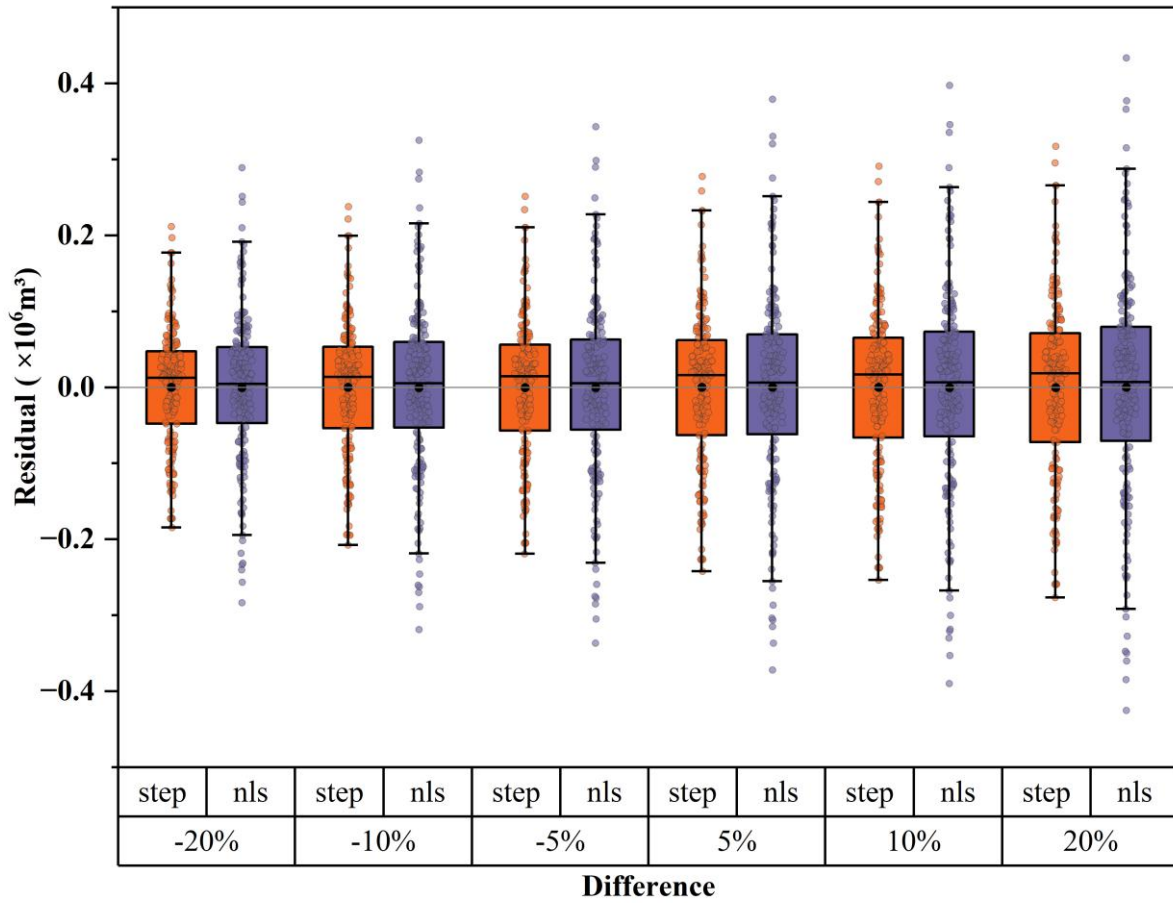
Figure 9. Residual distribution for two regression methods under three artificial error scenarios (±5%, ±10%, and ±20%). The black dots and black short lines of the box plots are the mean and median of the residuals, respectively; the whiskers denote 1.5 times the IQR from both ends of the box.

4.3 Limitations of statistical regression methods

There is still a lack of studies on the physical theories of the formation of each morphological characteristic, which hinders us from proposing an ideal nonlinear statistical regression model framework, even after several attempts. For instance, we tried to consider the effect of ice temperature on erosion intensity by incorporating normalized elevation as well as more complex regression models from the physical symbolic optimization (PhySO) framework, but their performance did not improve evidently compared to our simple regression models. According to a theoretical model of channel meander formation (Karlstrom et al., 2013), for a given supraglacial channel with a fixed cross section, runoff, and ice temperature, a bender channel meander tends to produce more heat by flowing water, which favors ice melting and lateral migration at the vertex. This implies that, in addition to the influence of external forces, such as water discharge, the channel morphology itself has a complex self-feedback process. Although Pitcher and Smith (2019) emphasized the importance of integrating thermal forcing

376 models (ice and water temperature), topography, and hydraulic parameters because they are helpful in understanding the

377 physical mechanism behind the formation of supraglacial river systems, the framework of physical-based models or more

378 appropriate forms of nonlinear models that can help improve the performance of predicted discharge using only the geometric

379 parameters of channels are still unavailable.

4.4 Applicability and perspective of regression model

381 The Qiyi Glacier is a typical subcontinental glacier on the Tibetan Plateau with weak subglacial hydrological processes. As a

382 result, meltwater mainly originates from the glacier surface and flows across the surface, forming a relatively continuous

383 channel network. ~~Thus, we infer that this approach is well suited to polythermal or cold-based glaciers with limited subglacial~~

384 ~~hydrological activity or surface structures. However, it may be less applicable to maritime glaciers with large crevasses or~~

385 ~~numerous active moulins, such as those on the southern Tibetan Plateau and the Greenland Ice Sheet.~~ ~~The model proposed in~~

386 ~~this study provides a valuable reference for quantifying the annual discharge of this type of glacier.~~

387 ~~However, the applicability of this approach is limited for some other glacier types. For example, on maritime glaciers with~~

388 ~~extensive crevasses and relatively stronger subglacial hydrological processes (e.g., in the southern Tibetan Plateau and the~~

389 ~~Greenland Ice Sheet), some supraglacial rivers often terminate in crevasses or moulins, which makes our regression model~~

390 ~~less suitable for estimating glacier runoff. Similarly, temperate glaciers, debris covered glaciers, and glaciers with strong~~

391 ~~surface structures are likely too complex to be represented without substantial modifications to the model.~~ But the model still

392 has positive implications for supraglacial river segments between crevasses and moulins. The drainage areas of supraglacial

393 river segments can be obtained by watershed delineation, and the meltwater discharge of each drainage area can be estimated

394 from their geometry.

395 It should also be emphasized that, while channel geometric parameters can be derived from remote sensing data alone, the

396 establishment of this regression model require mass balance data for calibrating the coefficients in runoff estimation due to

397 scaling differences among glaciers. Therefore, the broader application of this method to other glaciers must be accompanied

398 by reliable mass balance data.

5 Conclusions

400 Accurate estimation of glacier meltwater runoff is of great importance for quantifying the effects of climate change on glacier

401 dynamics and evaluating the impacts of glacier changes on downstream water resource security. Based on high-precision UAV

402 orthophotos and LiDAR data, this study derived a comprehensive supraglacial channel network over the Qiyi Glacier for the

403 first time, from which a series of channel morphological characteristics were used to predict the meltwater discharge using

404 different regression methods. Compared with traditional methods based on field observations or glacier runoff models, our

405 study provides a novel perspective for accurately estimating annual glacier discharge for larger glaciated areas without

406 meteorological and hydrological observations. The stepwise regression model incorporating the parameters of lateral deviation,

channel gradient, and width of the supraglacial channel performed better, explaining approximately 78.2% of the variation in the observed meltwater discharge. The regression accuracy improved to 81.8% after the five-point moving average filtering. The NLS regression model using only the more readily available parameters of lateral deviation and channel gradient performed slightly less well, explaining 66.2% of the variation in meltwater discharge, whereas the explained variance was improved to 81.4% after applying a five-point moving average. In recent years, centimeter-scale multi-satellite constellations with predominantly onboard optical sensors, such as the WorldView Legion satellites, Pelican-2 satellite, and Gen-3 constellation, have become an important development trend. Our study indicated that although the skill of the stepwise regression model incorporating lateral deviation, channel gradient, and width was higher than that of the NLS regression model using only lateral deviation and channel gradient, their performances were nearly the same after five-point moving average filtering. When using centimeter- scale resolution satellite remote sensing data to predict glacier meltwater yield over larger areas, it is recommended to use a nonlinear fitting model with a minimum amount of input data and higher reliability.

Author Contribution

Conceptualisation: YW. Methodology: LX, YW, AC. Investigation: LX, YW, AC. Project administration: NW, SZ. Resources: NW, SZ. Software: HS. Visualisation: LX, HS. Writing (original draft): LX. Writing (review and editing): YW.

Competing interests

The contact author has declared that none of the authors has any competing interests.

Data Availability Statement

The UAV-processed data (orthomosaic and DEM), supraglacial channel line vectors, and regression data (including geometric parameters and regression results) are available online (Xie and Wu, 2025).

Acknowledgements

This work was supported by the National Natural Science Foundation of China (Grant No. 42171139, 42130516), the Second Tibetan Plateau Scientific Expedition and Research Program (2019QZKK020102), and the Open Research Fund of National Cryosphere Desert Data Center (Grant No.2024NCDC001).

References

Beamer, J. P., Hill, D. F., Arendt, A., and Liston, G. E.: High-resolution modeling of coastal freshwater discharge and glacier mass balance in the Gulf of Alaska watershed, Water Resour. Res., 52, 3888–3909, https://doi.org/10.1002/2015WR018457, 2016.

Bell, R. E., Chu, W., Kingslake, J., Das, I., Tedesco, M., Tinto, K. J., Zappa, C. J., Frezzotti, M., Boghosian, A., and Lee, W. S.: Antarctic ice shelf potentially stabilized by export of meltwater in surface river, Nature, 544, 344–348, https://doi.org/10.1038/nature22048, 2017.

Bergstrom, A., Gooseff, M., Fountain, A., and Hoffman, M.: Long-term shifts in feedbacks among glacier surface change, melt generation and runoff, MCMURDO Dry Valleys, Antarctica, Hydrol. Process., 35, e14292, https://doi.org/10.1002/hyp.14292, 2021.

Bhardwaj, A., Sam, L., Akanksha, Martín-Torres, F. J., and Kumar, R.: UAVs as remote sensing platform in glaciology: Present applications and future prospects, Remote Sens. Environ., 175, 196–204, https://doi.org/10.1016/j.rse.2015.12.029, 2016.

Bjerklie, D. M., Birkett, C. M., Jones, J. W., Carabajal, C., Rover, J. A., Fulton, J. W., and Garambois, P.-A.: Satellite remote sensing estimation of river discharge: Application to the Yukon River Alaska, J. Hydrol., 561, 1000–1018, https://doi.org/10.1016/j.jhydrol.2018.04.005, 2018.

Bolch, T., Kulkarni, A., Kääb, A., Huggel, C., Paul, F., Cogley, J. G., Frey, H., Kargel, J. S., Fujita, K., Scheel, M., Bajracharya, S., and Stoffel, M.: The State and Fate of Himalayan Glaciers, Science, 336, 310–314, https://doi.org/10.1126/science.1215828, 2012.

Burns, P. and Nolin, A.: Using atmospherically-corrected Landsat imagery to measure glacier area change in the Cordillera Blanca, Peru from 1987 to 2010, Remote Sens. Environ., 140, 165–178, https://doi.org/10.1016/j.rse.2013.08.026, 2014.

Chen, J., Wang, N., Wu, Y., Chen, A., Shi, C., Zhao, M., and Xie, L.: Quantifying Qiyi Glacier Surface Dirtiness Using UAV and Sentinel-2 Imagery, Remote Sens., 16, https://doi.org/10.3390/rs16173351, 2024.

Colgan, W., Steffen, K., McLamb, W. S., Abdalati, W., Rajaram, H., Motyka, R., Phillips, T., and Anderson, R.: An increase in crevasse extent, West Greenland: Hydrologic implications, Geophys. Res. Lett., 38, https://doi.org/10.1029/2011GL048491, 2011.

Curran, J. H., Rick, B., Littell, J. S., and Sass, L. C.: Streamflow Response to Glacier Mass Loss Varies With Basin Precipitation Across Alaska, Water Resour. Res., 61, e2024WR037859, https://doi.org/10.1029/2024WR037859, 2025.

Dall'Asta, E., Forlani, G., Roncella, R., Santise, M., Diotri, F., and Cella, U. M. di: Unmanned Aerial Systems and DSM matching for rock glacier monitoring, ISPRS J. Photogramm. Remote Sens., 127, 102–114, https://doi.org/10.1016/j.isprsjprs.2016.10.003, 2017.

461   Dehecq, A., Gourmelen, N., Gardner, A. S., Brun, F., Goldberg, D., Nienow, P. W., Berthier, E., Vincent, C., Wagnon, P., and
462   Trouvé, E.: Twenty-first century glacier slowdown driven by mass loss in High Mountain Asia, Nat. Geosci., 12, 22–27,
463   https://doi.org/10.1038/s41561-018-0271-9, 2019.

464   Dyurgerov, M.: Glacier mass balance and regime: Data of measurements and analysis, Occasional Paper 55, Institute of Arctic
465   and Alpine Research, University of Colorado, Boulder, CO, 2022

466   Gleason, C. J., Smith, L. C., Chu, V. W., Legleiter, C. J., Pitcher, L. H., Overstreet, B. T., Rennermalm, A. K., Forster, R. R.,
467   and Yang, K.: Characterizing supraglacial meltwater channel hydraulics on the Greenland Ice Sheet from *in situ*
468   observations, Earth Surf. Process. Landf., 41, 2111–2122, https://doi.org/10.1002/esp.3977, 2016.

469   Hock, R.: Glacier melt: a review of processes and their modelling, Prog. Phys. Geogr., 29, 362–391, 2005.

470   Hugenholtz, C. H., Whitehead, K., Brown, O. W., Barchyn, T. E., Moorman, B. J., LeClair, A., Riddell, K., and Hamilton, T.:
471   Geomorphological mapping with a small unmanned aircraft system (sUAS): Feature detection and accuracy assessment
472   of a photogrammetrically-derived digital terrain model, Geomorphology, 194, 16–24,
473   https://doi.org/10.1016/j.geomorph.2013.03.023, 2013.

474   Huss, M.: Present and future contribution of glacier storage change to runoff from macroscale drainage basins in Europe,
475   Water Resour. Res., 47, https://doi.org/10.1029/2010WR010299, 2011.

476   Immerzeel, W. W., Kraaijenbrink, P. D. A., Shea, J. M., Shrestha, A. B., Pellicciotti, F., Bierkens, M. F. P., and de Jong, S.
477   M.: High-resolution monitoring of Himalayan glacier dynamics using unmanned aerial vehicles, Remote Sens. Environ.,
478   150, 93–103, https://doi.org/10.1016/j.rse.2014.04.025, 2014.

479   Immerzeel, W. W., Lutz, A. F., Andrade, M., Bahl, A., Biemans, H., Bolch, T., Hyde, S., Brumby, S., Davies, B. J., Elmore,
480   A. C., Emmer, A., Feng, M., Fernández, A., Haritashya, U., Kargel, J. S., Koppes, M., Kraaijenbrink, P. D. A., Kulkarni,
481   A. V., Mayewski, P. A., Nepal, S., Pacheco, P., Painter, T. H., Pellicciotti, F., Rajaram, H., Rupper, S., Sinisalo, A.,
482   Shrestha, A. B., Viviroli, D., Wada, Y., Xiao, C., Yao, T., and Baillie, J. E. M.: Importance and vulnerability of the
483   world's water towers, Nature, 577, 364–369, https://doi.org/10.1038/s41586-019-1822-y, 2020.

484   Jarosch, A. H. and Gudmundsson, M. T.: A numerical model for meltwater channel evolution in glaciers, The Cryosphere, 6,
485   493–503, https://doi.org/10.5194/tc-6-493-2012, 2012.

486   Jiang, X., Wang, N., He, J., Wu, X., and Song, G.: A distributed surface energy and mass balance model and its application to
487   a mountain glacier in China, Chin. Sci. Bull., 55, 2079–2087, https://doi.org/10.1007/s11434-010-3068-9, 2010.

488   Kääb, A., Berthier, E., Nuth, C., Gardelle, J., and Arnaud, Y.: Contrasting patterns of early twenty-first-century glacier mass
489   change in the Himalayas, Nature, 488, 495–498, https://doi.org/10.1038/nature11324, 2012.

490   Karlstrom, L., Gajjar, P., and Manga, M.: Meander formation in supraglacial streams, J. Geophys. Res. Earth Surf., 118, 1897–
491   1907, https://doi.org/10.1002/jgrf.20135, 2013.

492   Kaser, G., Cogley, J. G., Dyurgerov, M. B., Meier, M. F., and Ohmura, A.: Mass balance of glaciers and ice caps: Consensus
493   estimates for 1961–2004, Geophys. Res. Lett., 33, https://doi.org/10.1029/2006GL027511, 2006.

494 Knighton, A. D.: Asymmetry of river channel cross-sections: Part I. Quantitative indices, Earth Surf. Process. Landf., 6, 581–
495   588, https://doi.org/10.1002/esp.3290060607, 1981.

496 Kraaijenbrink, P., Meijer, S. W., Shea, J. M., Pellicciotti, F., De Jong, S. M., and Immerzeel, W. W.: Seasonal surface velocities
497   of a Himalayan glacier derived by automated correlation of unmanned aerial vehicle imagery, Ann. Glaciol., 57, 103–
498   113, https://doi.org/10.3189/2016AoG71A072, 2016.

499 Kraaijenbrink, P. D. A. and Immerzeel, W. W.: Spatial and Temporal Variability of the Surface Mass Balance of Debris-
500   Covered Glacier Tongues, J. Geophys. Res. Earth Surf., 130, e2024JF007935, https://doi.org/10.1029/2024JF007935,
501   2025.

502 Legleiter, C. J., Tedesco, M., Smith, L. C., Behar, A. E., and Overstreet, B. T.: Mapping the bathymetry of supraglacial lakes
503   and streams on the Greenland ice sheet using field measurements and high-resolution satellite images, The Cryosphere,
504   8, 215–228, https://doi.org/10.5194/tc-8-215-2014, 2014.

505 Muthyala, R., Rennermalm, Å. K., Leidman, S. Z., Cooper, M. G., Cooley, S. W., Smith, L. C., and van As, D.: Supraglacial
506   streamflow and meteorological drivers from southwest Greenland, The Cryosphere, 16, 2245–2263,
507   https://doi.org/10.5194/tc-16-2245-2022, 2022.

508 Nie, Y., Pritchard, H. D., Liu, Q., Hennig, T., Wang, W., Wang, X., Liu, S., Nepal, S., Samyn, D., Hewitt, K., and Chen, X.:
509   Glacial change and hydrological implications in the Himalaya and Karakoram, Nat. Rev. Earth Environ., 2, 91–106,
510   https://doi.org/10.1038/s43017-020-00124-w, 2021.

511 Paul, F., Bolch, T., Kääb, A., Nagler, T., Nuth, C., Scharrer, K., Shepherd, A., Strozzi, T., Ticconi, F., Bhambri, R., Berthier,
512   E., Bevan, S., Gourmelen, N., Heid, T., Jeong, S., Kunz, M., Lauknes, T. R., Luckman, A., Merryman Boncori, J. P.,
513   Moholdt, G., Muir, A., Neelmeijer, J., Rankl, M., VanLooy, J., and Van Niel, T.: The glaciers climate change initiative:
514   Methods for creating glacier area, elevation change and velocity products, Remote Sens. Environ., 162, 408–426,
515   https://doi.org/10.1016/j.rse.2013.07.043, 2015.

516 Pitcher, L. H. and Smith, L. C.: Supraglacial Streams and Rivers, Annu. Rev. Earth Planet. Sci., 47, 421–452,
517   https://doi.org/10.1146/annurev-earth-053018-060212, 2019.

518 Rabatel, A., Letréguilly, A., Dedieu, J.-P., and Eckert, N.: Changes in glacier equilibrium-line altitude in the western Alps
519   from 1984 to 2010: evaluation by remote sensing and modeling of the morpho-topographic and climate controls, The
520   Cryosphere, 7, 1455–1471, https://doi.org/10.5194/tc-7-1455-2013, 2013.

521 Ren, S., Jia, L., Miles, E. S., Menenti, M., Kneib, M., Shaw, T. E., Buri, P., McCarthy, M. J., Yang, W., Pellicciotti, F., and
522   Yao, T.: Observed and projected declines in glacier albedo across the Third Pole in the 21st century, One Earth, 7, 1587–
523   1599, https://doi.org/10.1016/j.oneear.2024.08.010, 2024.

524 Rippin, D. M., Pomfret, A., and King, N.: High resolution mapping of supra-glacial drainage pathways reveals link between
525   micro-channel drainage density, surface roughness and surface reflectance, Earth Surf. Process. Landf., 40, 1279–1290,
526   https://doi.org/10.1002/esp.3719, 2015.

527 Rodríguez–Iturbe, I., Ijjász-Vásquez, E. J., Bras, R. L., and Tarboton, D. G.: Power law distributions of discharge mass and
528   energy in river basins, Water Resour. Res., 28, 1089–1093, https://doi.org/10.1029/91WR03033, 1992.

529 Sicart, J. E., Hock, R., and Six, D.: Glacier melt, air temperature, and energy balance in different climates: The Bolivian
530   Tropics, the French Alps, and northern Sweden, J. Geophys. Res. Atmospheres, 113, 2008JD010406,
531   https://doi.org/10.1029/2008JD010406, 2008.

532 Śledź, S., Ewertowski, M. W., and Piekarczyk, J.: Applications of unmanned aerial vehicle (UAV) surveys and Structure from
533   Motion photogrammetry in glacial and periglacial geomorphology, Geomorphology, 378, 107620,
534   https://doi.org/10.1016/j.geomorph.2021.107620, 2021.

535 Smith, L. C., Chu, V. W., Yang, K., Gleason, C. J., Pitcher, L. H., Rennermalm, A. K., Legleiter, C. J., Behar, A. E., Overstreet,
536   B. T., Moustafa, S. E., Tedesco, M., Forster, R. R., LeWinter, A. L., Finnegan, D. C., Sheng, Y., and Balog, J.: Efficient
537   meltwater drainage through supraglacial streams and rivers on the southwest Greenland ice sheet, Proc. Natl. Acad. Sci.,
538   112, 1001–1006, https://doi.org/10.1073/pnas.1413024112, 2015.

539 Smith, L. C., Yang, K., Pitcher, L. H., Overstreet, B. T., Chu, V. W., Rennermalm, Å. K., Ryan, J. C., Cooper, M. G., Gleason,
540   C. J., Tedesco, M., Jeyaratnam, J., van As, D., van den Broeke, M. R., van de Berg, W. J., Noël, B., Langen, P. L.,
541   Cullather, R. I., Zhao, B., Willis, M. J., Hubbard, A., Box, J. E., Jenner, B. A., and Behar, A. E.: Direct measurements of
542   meltwater runoff on the Greenland ice sheet surface, Proc. Natl. Acad. Sci., 114, E10622–E10631,
543   https://doi.org/10.1073/pnas.1707743114, 2017.

544 Smith, L. C., Andrews, L. C., Pitcher, L. H., Overstreet, B. T., Rennermalm, Å. K., Cooper, M. G., Cooley, S. W., Ryan, J. C.,
545   Miège, C., Kershner, C., and Simpson, C. E.: Supraglacial River Forcing of Subglacial Water Storage and Diurnal Ice
546   Sheet Motion, Geophys. Res. Lett., 48, e2020GL091418, https://doi.org/10.1029/2020GL091418, 2021.

547 St Germain, S. L. and Moorman, B. J.: Long-term observations of supraglacial streams on an Arctic glacier, J. Glaciol., 65,
548   900–911, https://doi.org/10.1017/jog.2019.60, 2019.

549 Wang, K., Wu, Y., Qiu, X., Zhu, J., Zheng, D., Shangguan, S., Pan, J., Liu, Y., Jiang, L., and Li, X.: A novel airborne
550   TomoSAR 3-D focusing method for accurate ice thickness and glacier volume estimation, ISPRS J. Photogramm. Remote
551   Sens., 220, 593–607, https://doi.org/10.1016/j.isprsjprs.2025.01.011, 2025.

552 Wang, L., Yao, T., Chai, C., Cuo, L., Su, F., Zhang, F., Yao, Z., Zhang, Y., Li, X., Qi, J., Hu, Z., Liu, J., and Wang, Y.: TP-
553   River: Monitoring and Quantifying Total River Runoff from the Third Pole, Bull. Am. Meteorol. Soc., 102, E948–E965,
554   https://doi.org/10.1175/BAMS-D-20-0207.1, 2021.

555 Wang, L., Liu, H., Bhlon, R., Chen, D., Long, J., and Sherpa, T. C.: Modeling glacio-hydrological processes in the Himalayas:
556   A review and future perspectives, Geogr. Sustain., 5, 179–192, https://doi.org/10.1016/j.geosus.2024.01.001, 2024.

557 Wang, S., Yao, T., Tian, L., and Pu, J.: Glacier mass variation and its effect on surface runoff in the Beida River catchment
558   during 1957–2013, J. Glaciol., 63, 523–534, https://doi.org/10.1017/jog.2017.13, 2017.

Wu, Y., Wang, N., Li, Z., Chen, A., Guo, Z., and Qie, Y.: The effect of thermal radiation from surrounding terrain on glacier surface temperatures retrieved from remote sensing data: A case study from Qiyi Glacier, China, Remote Sens. Environ., 231, 111267, https://doi.org/10.1016/j.rse.2019.111267, 2019.

Xie, L. and Wu, Y.: Unmanned aerial vehicle data of Qiyi Glacier for 2023, https://doi.org/10.5281/zenodo.15314577, 2025.

Xu, C., Li, Z., Li, H., Wang, F., and Zhou, P.: Long-range terrestrial laser scanning measurements of annual and intra-annual mass balances for Urumqi Glacier No. 1, eastern Tien Shan, China, The Cryosphere, 13, 2361–2383, https://doi.org/10.5194/tc-13-2361-2019, 2019.

Xu, J., Wang, L., Yao, T., Chen, D., Wang, G., Jing, Z., Zhang, F., Wang, Y., Li, X., Zhang, Y., Wang, Y., Zeng, T., Chai, C., Liu, H., Liu, R., Long, J., Fan, X., Bhlon, R., and Xu, B.: Totaling river discharge of the third pole from satellite imagery, Remote Sens. Environ., 308, 114181, https://doi.org/10.1016/j.rse.2024.114181, 2024.

Xu, M., Wang, P., Zhang, X., Ma, T., Jin, J., Kang, S., Han, H., Wu, H., Hou, Z., Li, X., and Wu, X.: Impacts of glacier shrinkage on peak melt runoff at the sub-basin scale of Northwest China, J. Hydrol., 654, 132953, https://doi.org/10.1016/j.jhydrol.2025.132953, 2025.

Xue, Y., Hong, X., He, X., Kang, S., Wang, S., and Ding, Y.: An evaluation of TLS-based glacier change assessment in the central Tibetan plateau, Int. J. Digit. Earth, 17, 2375527, https://doi.org/10.1080/17538947.2024.2375527, 2024.

Yang, K. and Smith, L. C.: Internally drained catchments dominate supraglacial hydrology of the southwest Greenland Ice Sheet, J. Geophys. Res. Earth Surf., 121, 1891–1910, https://doi.org/10.1002/2016JF003927, 2016.

Yang, K., Smith, L. C., Fettweis, X., Gleason, C. J., Lu, Y., and Li, M.: Surface meltwater runoff on the Greenland ice sheet estimated from remotely sensed supraglacial lake infilling rate, Remote Sens. Environ., 234, 111459, https://doi.org/10.1016/j.rse.2019.111459, 2019.

Yang, Z., Bai, P., Tian, Y., and Liu, X.: Glacier Coverage Dominates the Response of Runoff and Its Components to Climate Change in the Tianshan Mountains, Water Resour. Res., 61, e2024WR037947, https://doi.org/10.1029/2024WR037947, 2025.

Yao, T., Bolch, T., Chen, D., Gao, J., Immerzeel, W., Piao, S., Su, F., Thompson, L., Wada, Y., Wang, L., Wang, T., Wu, G., Xu, B., Yang, W., Zhang, G., and Zhao, P.: The imbalance of the Asian water tower, Nat. Rev. Earth Environ., 3, 618–632, https://doi.org/10.1038/s43017-022-00299-4, 2022.

Zemp, M., Huss, M., Thibert, E., Eckert, N., McNabb, R., Huber, J., Barandun, M., Machguth, H., Nussbaumer, S. U., Gärtner-Roer, I., Thomson, L., Paul, F., Maussion, F., Kutuzov, S., and Cogley, J. G.: Global glacier mass changes and their contributions to sea-level rise from 1961 to 2016, Nature, 568, 382–386, https://doi.org/10.1038/s41586-019-1071-0, 2019.

Zhang, W., Yang, K., Smith, L. C., Wang, Y., van As, D., Noël, B., Lu, Y., and Liu, J.: Pan-Greenland mapping of supraglacial rivers, lakes, and water-filled crevasses in a cool summer (2018) and a warm summer (2019), Remote Sens. Environ., 297, 113781, https://doi.org/10.1016/j.rse.2023.113781, 2023.